Table 3: Hemodynamic parameters, blood flow volume of the SMA, and resistive index of retrobulbar arteries by acupuncture on ST36. The values represent the mean and SD. $^{*}P < 0.05$, $^{**}P < 0.01$ versus before acupuncture.

Parameters	Acupuncture on ST36	
	Before	After
Systolic blood pressure (mmHg)	121.7 ± 11.8	120.7 ± 10.9
Diastolic blood pressure (mmHg)	77.8 ± 9.4	77.6 ± 7.6
Heart rate (beats/min)	61.9 ± 6.6	61.5 ± 7.4
Blood flow volume of the SMA (mL/min)	549.8 ± 192.2	620.2 ± 188.1*
RI in OA	0.736 ± 0.07	0.728 ± 0.070
RI in CRA	0.617 ± 0.065	0.631 ± 0.043
RI in SPCA	0.600 ± 0.030	0.580 ± 0.06

Table 4: Hemodynamic parameters and resistive index of retrobulbar arteries in control and acupuncture therapy. The values represent the mean and SD. $^{*}P < 0.05$, $^{**}P < 0.01$ versus rest or before acupuncture. $^{\dagger}P < 0.05$, $^{\dagger\dagger}P < 0.01$ versus control. Modified from [2].

Parameters	Control		Acupuncture	
	Rest	After 1 hour	Before	After
Systolic blood pressure (mmHg)	116.4 ± 10.0	119.8 ± 7.6	124.5 ± 12.9	122.6 ± 9.7
Diastolic blood pressure (mmHg)	69.8 ± 6.5	68.6 ± 3.9	74.5 ± 5.4	72.0 ± 2.9
Heart rate (beats/min)	61.5 ± 7.3	60.1 ± 8.1	61.7 ± 8.5	60.3 ± 10.4
RI in OA	0.74 ± 0.04	0.75 ± 0.05	0.74 ± 0.04	0.74 ± 0.04
RI in CRA	0.75 ± 0.09	0.72 ± 0.03	0.72 ± 0.05	0.68 ± 0.04*
RI in SPCA	0.68 ± 0.05	0.68 ± 0.04	0.67 ± 0.04	0.64 ± 0.06*††

mechanisms. The present result suggests that LR3 located on the foot and apart from the eye can affect the circulation in the retrobulbar arteries.

3.3. Experiment 3: Effects of ST36 Acupuncture on Blood Circulation to the Eye and through the SMA. RI in the retrobulbar vessels was not changed by ST36 acupuncture treatment. However, the blood flow volume in the SMA was significantly greater after acupuncture than before ($P < 0.05$; Table 3). Acupuncture on the limbs was also demonstrated to elicit systemic visceral responses via the supraspinal reflexes in animal models [9, 36, 37]. According to several reports, blood flow volume in the SMA increased significantly after stimulation of the lower limbs [9, 36–38]. We speculate that this increase is caused by excitation of the parasympathetic system and inhibition of the sympathetic system via supraspinal reflexes. The present result suggests that ST36 located on the lower limb and apart from the abdomen can affect the circulation in the SMA.

3.4. Experiment 4: Effects of Acupuncture on Retrobulbar Circulation in OAG Patients. RI in the CRA and SPCA were significantly lower after acupuncture than it was before acupuncture treatment (CRA; $P < 0.05$, SPCA; $P < 0.05$; Table 4). RI in the SPCA was also significantly lower after acupuncture than when no treatment was given (SPCA; $P < 0.01$; Table 4). The CRA supplies blood to the retina and SPCA, to the choroid (Figure 4). The decrease of the distal vascular resistance in the CRA and SPCA that we observed indicates that acupuncture results in an increase of the blood flow to the retina and choroid. The possible physiological mechanisms of increase blood flow in eye has already described in the discussion of Experiment 2. The present result suggests that acupuncture can improve the retrobulbar circulation in the patients of OAG with standard medication.

4. Ultrasound and CDI

4.1. Advantage. We focused on the evaluation of CDI by ultrasound. Noninvasive and real-time measure of CDI was applied to assess circulation in organs after acupuncture. The continuous method of CDI was used to assess the brief effects of circulation in the arm (Experiment 1). The simultaneous evaluation by CDI was applied to assess the circulation in two different organs (Experiments 2 and 3). Resistive index measured by CDI is measured in the small vessels as retrobulbar arteries (Experiment 4). Acupuncture affects the autonomic nervous system via the somatic nerves. Invasive evaluation also affects these systems and reflex. Therefore, invasive evaluation might not correctly evaluate the physiological effects of acupuncture therapy. We suggest that real-time and noninvasive hemodynamic measurement as CDI is suitable to measure the physiological effects in humans.

4.2. Limitation. While CDI provides detailed images of blood vessels in real-time, there are limits to the hemodynamic measurements that can be made using this technique. In addition, while CDI is useful for the measurement of blood flow in various vessels in real time, it does not have sufficient resolution to determine the diameter of very small retrobulbar vessels such as OA, CRA, and SPCA. Therefore,

CDI cannot be used to measure blood flow volume in these vessels. However, it can provide an index of vascular resistance such as RI. A decrease in the distal vascular resistance in the small vessels indicates an increase in the blood flow in the distal part of the vessels. Additionally, care must be taken to avoid compression of the eyeball during ultrasound examination. Such compression is likely to cause intraocular pressure elevation and trigger the vagal reflex. Measurement of blood flow in the retrobulbar arteries requires attention to probe maintenance and careful avoidance of pressure on the eyeball [23]. Expert technique is required to obtain reproducible results using CDI. In addition to the limits of CDI resolution, ultrasound waves that strike blood vessels at angles greater than 60° relative to the direction of blood flow result in a large margin of error for CDI measurements. Therefore, it is important to measure blood flow at a Doppler angle of less than 60 degrees [34, 35].

4.3. Further Study. The other methods to assess the physiological changes by acupuncture noninvasively are impedance cardiography and spectral analysis of heart rate variability. Impedance cardiography is a noninvasive monitoring method that allows measurement of the cardiac index based on the changes in thoracic resistance that results from variations in intrathoracic blood flow volume [39, 40]. Spectral analysis of heart rate variability is useful to evaluate the autonomic nervous balance noninvasively [41, 42]. Combined with these measurements, we can clarify the mechanism of increased blood flow volume in several organs in humans. In the future, we would like to explore the efficacy of acupuncture as treatment for various diseases by using diagnostic tools, such as CDI.

5. Conclusion

CDI can noninvasively depict blood vessels in the human body, and can quantitatively evaluate blood flow in real time. Our studies showed the changes of blood flow in the peripheral, mesenteric, and retrobulbar arteries by acupuncture estimated by CDI. This technique is suitable as an evaluation method to consider physiological changes due to acupuncture as blood flow changes.

Conflict of Interests

The authors have no conflict of interests.

Acknowledgments

Experiment 1 was supported by Special Coordination Funds for Promoting Science and Technology from the Japanese Ministry of Education, Culture, Sports, Science and Technology. Experiment 4 was supported by Health and Labour Sciences Research Grants for Clinical Research from the Japanese Ministry of Health, Labour and Welfare.

References

[1] S. Takayama, T. Seki, M. Watanabe et al., "Brief effect of acupuncture on the peripheral arterial system of the upper limb and systemic hemodynamics in humans," *Journal of Alternative and Complementary Medicine*, vol. 16, no. 7, pp. 707–713, 2010.

[2] S. Takayama, T. Seki, T. Nakazawa et al., "Short-term effects of acupuncture on open-angle glaucoma in retrobulbar circulation: additional therapy to standard medication," *Evidence-Based Complementary and Alternative Medicine*, vol. 2011, Article ID 157090, 6 pages, 2011.

[3] S. Takayama, T. Seki, M. Watanabe et al., "Changes of blood flow volume in the superior mesenteric artery and brachial artery with abdominal thermal stimulation," *Evidence-Based Complementary and Alternative Medicine*, vol. 2011, Article ID 214089, 10 pages, 2011.

[4] S. Takayama, T. Seki, N. Sugita et al., "Radial artery hemodynamic changes related to acupuncture," *Explore*, vol. 6, no. 2, pp. 100–105, 2010.

[5] S. Takayama, T. Seki, M. Watanabe et al., "The effect of warming of the abdomen and of herbal medicine on superior mesenteric artery blood flow—a pilot study," *Forschende Komplementarmedizin*, vol. 17, no. 4, pp. 195–201, 2010.

[6] D. Irnich and A. Beyer, "Neurobiological mechanisms of acupuncture analgesia," *Schmerz*, vol. 16, no. 2, pp. 93–102, 2002.

[7] J. G. Lin and W. L. Chen, "Acupuncture analgesia: a review of its mechanisms of actions," *American Journal of Chinese Medicine*, vol. 36, no. 4, pp. 635–645, 2008.

[8] Z. Q. Zhao, "Neural mechanism underlying acupuncture analgesia," *Progress in Neurobiology*, vol. 85, no. 4, pp. 355–375, 2008.

[9] S. Uchida and H. Hotta, "Acupuncture affects regional blood flow in various organs," *Evidence-Based Complementary and Alternative Medicine*, vol. 5, no. 2, pp. 145–151, 2008.

[10] H. Tsuru and K. Kawakita, "Acupuncture on the blood flow of various organs measured simultaneously by colored microspheres in rats," *Evidence-Based Complementary and Alternative Medicine*, vol. 6, no. 1, pp. 77–83, 2009.

[11] E. Haker, H. Egekvist, and P. Bjerring, "Effect of sensory stimulation (acupuncture) on sympathetic and parasympathetic activities in healthy subjects," *Journal of the Autonomic Nervous System*, vol. 79, no. 1, pp. 52–59, 2000.

[12] Y. Syuu, H. Matsubara, T. Kiyooka et al., "Cardiovascular beneficial effects of electroacupuncture at Neiguan (PC-6) acupoint in anesthetized open-chest dog," *Japanese Journal of Physiology*, vol. 51, no. 2, pp. 231–238, 2001.

[13] J. Soga, K. Nishioka, S. Nakamura et al., "Measurement of flow-mediated vasodilation of the brachial artery—a comparison of measurements in the seated and supine positions," *Circulation Journal*, vol. 71, no. 5, pp. 736–740, 2007.

[14] J. Deanfield, A. Donald, C. Ferri et al., "Endothelial function and dysfunction. Part I: methodological issues for assessment in the different vascular beds: a statement by the working group on endothelin and endothelial factors of the European society of hypertension," *Journal of Hypertension*, vol. 23, no. 1, pp. 7–17, 2005.

[15] J. Kjeldsen and O. B. Schaffalitzky de Muckadell, "Assessment of disease severity and activity in inflammatory bowel disease," *Scandinavian Journal of Gastroenterology*, vol. 28, no. 1, pp. 1–9, 1993.

[16] M. J. Perko, "Duplex ultrasound for assessment of superior mesenteric artery blood flow," *European Journal of Vascular and Endovascular Surgery*, vol. 21, no. 2, pp. 106–117, 2001.

[17] G. L. Moneta, D. C. Taylor, W. S. Helton, M. W. Mulholland, and D. E. Strandness, "Duplex ultrasound measurement of postprandial intestinal blood flow: effect of meal composition," *Gastroenterology*, vol. 95, no. 5, pp. 1294–1301, 1988.

[18] A. Erden, T. Cumhur, and T. Ölçer, "Superior mesenteric artery Doppler waveform changes in response to inflammation of the ileocecal region," *Abdominal Imaging*, vol. 22, no. 5, pp. 483–488, 1997.

[19] M. F. Byrne, M. A. Farrell, S. Abass et al., "Assessment of Crohn's disease activity by Doppler sonography of the superior mesenteric artery, clinical evaluation and the Crohn's disease activity index: a prospective study," *Clinical Radiology*, vol. 56, no. 12, pp. 973–978, 2001.

[20] A. Sigirci, T. Baysal, R. Kutlu et al., "Doppler sonography of the inferior and superior mesenteric arteries in ulcerative colitis," *Journal of Clinical Ultrasound*, vol. 29, no. 3, pp. 130–139, 2001.

[21] C. R. Deane and H. S. Markus, "Colour velocity flow measurement: in vitro validation and application to human carotid arteries," *Ultrasound in Medicine and Biology*, vol. 23, no. 3, pp. 447–452, 1997.

[22] U. Gembruch, "Assessment of the fetal circulatory state in uteroplacental insufficiency by Doppler ultrasound: which vessels are the most practicable?" *Ultrasound in Obstetrics and Gynecology*, vol. 8, no. 2, pp. 77–81, 1996.

[23] E. T. Matthiessen, O. Zeitz, G. Richard, and M. Klemm, "Reproducibility of blood flow velocity measurements using colour decoded Doppler imaging," *Eye*, vol. 18, no. 4, pp. 400–405, 2004.

[24] D. Bensky and J. O'Connor, *Acupuncture a Comprehensive Text*, Eastland Press, Seattle, Wash, USA, 1981.

[25] M. Giovanni, *The Moundations of Chinese Medicine*, Churchill Livingstone, Philadelphia, Pa, USA, 1989.

[26] Y. Yamazaki and S. M. Drance, "The relationship between progression of visual field defects and retrobulbar circulation in patients with glaucoma," *American Journal of Ophthalmology*, vol. 124, no. 3, pp. 287–295, 1997.

[27] I. Stalmans, A. Harris, S. Fieuws et al., "Color Doppler imaging and ocular pulse amplitude in glaucomatous and healthy eyes," *European Journal of Ophthalmology*, vol. 19, no. 4, pp. 580–587, 2009.

[28] M. Satilmis, S. Orgül, B. Doubler, and J. Flammer, "Rate of progression of glaucoma correlates with retrobulbar circulation and intraocular pressure," *American Journal of Ophthalmology*, vol. 135, no. 5, pp. 664–669, 2003.

[29] J. Schumann, S. Orgül, K. Gugleta, B. Dubler, and J. Flammer, "Interocular difference in progression of glaucoma correlates with interocular differences in retrobulbar circulation," *American Journal of Ophthalmology*, vol. 129, no. 6, pp. 728–733, 2000.

[30] R. W. Gill, "Measurement of blood flow by ultrasound: accuracy and sources of error," *Ultrasound in Medicine and Biology*, vol. 11, no. 4, pp. 625–641, 1985.

[31] F. Van Bel, P. H. T. Van Zwieten, G. L. Guit, and J. Schipper, "Superior mesenteric artery blood flow velocity and estimated volume flow: duplex Doppler US study of preterm and term neonates," *Radiology*, vol. 174, no. 1, pp. 165–169, 1990.

[32] K. Mayumi, "Aiming at a wide range of applications from preventive medicine to treatment," *Innervision*, vol. 21, no. 4, pp. 20–21, 2006.

[33] O. Takashi, "Measurement of minimal changes in blood vessels and its application," *Journal of Clinical Echocardiography*, vol. 7, no. 11, pp. 936–941, 2006.

[34] P. N. Burns and C. C. Jaffe, "Quamtitative flow measurements with Doppler ultrasound: techniques, accuracy, and limitations," *Radiologic Clinics of North America*, vol. 23, no. 4, pp. 641–657, 1985.

[35] K. J. W. Taylor and S. Holland, "Doppler US. Part I. Basic principles, instrumentation, and pitfalls," *Radiology*, vol. 174, no. 2, pp. 297–307, 1990.

[36] A. Sato, Y. Sato, A. Suzuki, and S. Uchida, "Reflex modulation of catecholamine secretion and adrenal sympathetic nerve activity by acupuncture-like stimulation in anesthetized rat," *Japanese Journal of Physiology*, vol. 46, no. 5, pp. 411–421, 1996.

[37] E. Noguchi, "Mechanism of reflex regulation of the gastroduodenal function by acupuncture," *Evidence-Based Complementary and Alternative Medicine*, vol. 5, no. 3, pp. 251–256, 2008.

[38] M. Watanabe, S. Takayama, T. Seki et al., "Haemodynamic changes in the superior mesenteric artery induced by acupuncture stimulation on the lower limbs," *Evidence-Based Complementary and Alternative Medicine*. In press.

[39] A. C. Perrino, A. Lippman, C. Ariyan, T. Z. O'Connor, and M. Luther, "Intraoperative cardiac output monitoring: comparison of impedance cardiography and thermodilution," *Journal of Cardiothoracic and Vascular Anesthesia*, vol. 8, no. 1, pp. 24–29, 1994.

[40] N. M. Albert, M. D. Hail, J. Li, and J. B. Young, "Equivalence of the bioimpedance and thermodilution methods in measuring cardiac output in hospitalized patients with advanced, decompensated chronic heart failure," *American Journal of Critical Care*, vol. 13, no. 6, pp. 469–479, 2004.

[41] S. Lee, Y. Chae, S. N. Kim et al., "Short term effects by acupuncture to SP3 on the autonomic blood flow control," *Neurological Research*, vol. 32, no. 1, pp. S37–S42, 2010.

[42] J. H. Lee, K. H. Kim, J. W. Hong, W. C. Lee, and S. Koo, "Comparison of electroacupuncture frequency-related effects on heart rate variability in healthy volunteers: a randomized clinical trial," *Journal of Acupuncture and Meridian Studies*, vol. 4, no. 2, pp. 107–115, 2011.

INTERNATIONAL JOURNAL FOR NUMERICAL METHODS IN BIOMEDICAL ENGINEERING
Int. J. Numer. Meth. Biomed. Engng. (2012)
Published online in Wiley Online Library (wileyonlinelibrary.com). DOI: 10.1002/cnm.2522

Reproduction of pressure field in ultrasonic-measurement-integrated simulation of blood flow

Kenichi Funamoto*,† and Toshiyuki Hayase

Institute of Fluid Science, Tohoku University, 2-1-1 Katahira, Aoba-ku, Sendai 980-8577, Japan

SUMMARY

Ultrasonic-measurement-integrated (UMI) simulation of blood flow is used to analyze the velocity and pressure fields by applying feedback signals of artificial body forces based on differences of Doppler velocities between ultrasonic measurement and numerical simulation. Previous studies have revealed that UMI simulation accurately reproduces the velocity field of a target blood flow, but that the reproducibility of the pressure field is not necessarily satisfactory. In the present study, the reproduction of the pressure field by UMI simulation was investigated. The effect of feedback on the pressure field was first examined by theoretical analysis, and a pressure compensation method was devised. When the divergence of the feedback force vector was not zero, it influenced the pressure field in the UMI simulation while improving the computational accuracy of the velocity field. Hence, the correct pressure was estimated by adding pressure compensation to remove the deteriorating effect of the feedback. A numerical experiment was conducted dealing with the reproduction of a synthetic three-dimensional steady flow in a thoracic aneurysm to validate results of the theoretical analysis and the proposed pressure compensation method. The ability of the UMI simulation to reproduce the pressure field deteriorated with a large feedback gain. However, by properly compensating the effects of the feedback signals on the pressure, the error in the pressure field was reduced, exhibiting improvement of the computational accuracy. It is thus concluded that the UMI simulation with pressure compensation allows for the reproduction of both velocity and pressure fields of blood flow. Copyright © 2012 John Wiley & Sons, Ltd.

Received 10 April 2012; Revised 27 July 2012; Accepted 21 September 2012

KEY WORDS: bio-fluid mechanics; computational fluid dynamics; ultrasonic measurement; color Doppler imaging; measurement-integrated simulation

1. INTRODUCTION

Circulatory diseases such as heart disease and cerebrovascular disease are major causes of death. *In vivo* and *in vitro* experiments and numerical simulations of blood flow have been extensively carried out, indicating the relationships between diseases and hemodynamics [1, 2]. Blood flow information acquired by medical imaging techniques, such as ultrasonic measurement, magnetic resonance imaging (MRI) and computed tomography (CT), or directly measured by a catheter, sphygmomanometer or electrocardiogram is limited. On the other hand, blood flow simulation provides detailed information on three-dimensional unsteady hemodynamics including wall shear stress and pressure distributions. However, as it is inherently difficult to correctly specify the boundary and initial conditions, the computational results may differ from the real blood flow field data [3,4]. Several methods have been proposed for flow simulation using defective boundary conditions, in which only flow rates are known [5, 6]. However, their efficiency for blood flow in a complicated

*Correspondence to: Kenichi Funamoto, Institute of Fluid Science, Tohoku University, 2-1-1 Katahira, Aoba-ku, Sendai 980-8577, Japan.

†E-mail: funamoto@reynolds.ifs.tohoku.ac.jp

vessel configuration remains to be investigated. Other factors, such as assumption of a rigid vessel wall, and uncertainties in vessel geometry, physical properties, and the model of the blood rheology, can also introduce errors into the computation. Consequently, at present, the diagnosis of circulatory diseases depends on empirical knowledge with limited measurement data. An innovative technique for accurate and detailed reproduction of blood flow field in a blood vessel is needed to realize more accurate and reliable diagnoses.

Various methodologies have been developed to computationally reproduce a flow field by integrating measurement and computation to overcome individual disadvantages. These methods include a method using proper orthogonal decomposition [7,8], data assimilation based on Tichonov regularization [9], least-squares finite element methods [10, 11], the Kalman filter [12], variational methods [13, 14], and measurement-integrated (MI) simulation [15–18]. Data assimilation based on four-dimensional variation is widely used, especially in numerical weather forecasting [14]. However, it requires huge computational resources to repeatedly solve flow dynamics and its adjoint, and therefore, is not suitable for application to problems of real-time flow reproduction. In contrast, the Kalman filter and MI simulation are rather simple methods sequentially comparing the computational result with the corresponding measurement data and directly feeding back the differences to the numerical simulation. Compared with the Kalman filter, which usually employs a low-dimensional linear model, the MI simulation, which uses computational fluid dynamics as a mathematical model, can provide a solution with high accuracy once a convergent result is obtained although there is no systematic design method of the feedback signal. The authors have applied MI simulation to blood flow analysis by integrating medical measurement (ultrasonic measurement or phase-contrast MRI) and numerical simulation [19,20]. With ultrasonic-measurement-integrated (UMI) simulation, the blood flow field is analyzed by applying artificial body forces proportional to the differences between the measured and computed Doppler velocities of the blood flow. Figure 1 shows a block diagram of the UMI simulation. Note that a 'Pressure compensation' block is newly added in this paper as explained in the following section. In our previous studies, a two-dimensional UMI simulation using real ultrasound color Doppler images was conducted [19]. The transient and steady characteristics of UMI simulation and the efficiency of feedback to reproduce unsteady three-dimensional hemodynamics were investigated by numerical experiments [21–23]. Those studies revealed that the UMI simulation improved computational accuracy in comparison with the ordinary simulation, making the computational velocity vector field approach that of a model solution of real blood flow. However, the reproducibility of the pressure field was not necessarily satisfactory [21,24].

In this study, reproduction of the pressure field by UMI simulation was investigated. In the second section of this paper, the effect of feedback based on Doppler velocity on the pressure field is first examined by theoretical analysis, and a pressure compensation method is derived. In the third section, results of the theoretical analysis and the proposed pressure compensation method are validated by a numerical experiment dealing with a synthetic three-dimensional steady flow in a thoracic aneurysm.

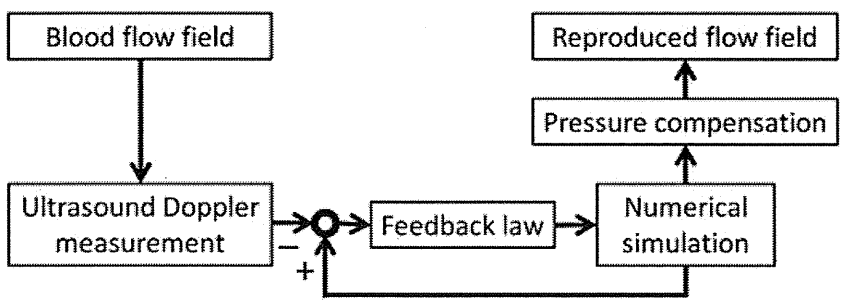

Figure 1. Block diagram of the UMI simulation.

DOI: 10.1002/cnm

2. THEORETICAL ANALYSIS

The effect of the feedback signal on the pressure field in the UMI simulation is clarified by theoretical analysis, and a pressure compensation method is developed.

2.1. *Effect of feedback signals on the pressure field*

The governing equations of the UMI simulation of blood flow in a blood vessel are the Navier–Stokes equations and the equation of continuity.

$$\rho\left(\frac{\partial \mathbf{u}}{\partial t}+(\mathbf{u}\cdot\nabla)\,\mathbf{u}\right)=\mu\Delta\mathbf{u}-\nabla p+\mathbf{f}, \tag{1}$$

$$\nabla\cdot\mathbf{u}=0, \tag{2}$$

where $\mathbf{u}=(u,\ v,\ w)$ is the velocity vector, p is the pressure, ρ is the density, μ is the viscosity, t is the time, and $\mathbf{f}=(f_x,\ f_y,\ f_z)$ is the external force term corresponding to the feedback signal. By substituting Equation (2) into the divergence of Equation (1), the pressure equation is derived as follows:

$$\Delta p=-\nabla\cdot\rho(\mathbf{u}\cdot\nabla)\,\mathbf{u}+\nabla\cdot\mathbf{f}. \tag{3}$$

Equations (1) and (3) are employed as the governing equations in the following analysis.

Regarding the boundary conditions, correct velocity profiles are assumed to be unknown, and a uniform or parabolic parallel profile with a known flow volume and free flow condition are specified at the upstream and downstream boundaries, respectively. The initial flow condition is an arbitrary flow field.

The feedback signal, $\mathbf{f}$, in Equation (1) is an artificial body force, which is proportional to the difference between the computed and measured Doppler velocities in the feedback domain defined in the computational domain:

$$\mathbf{f}=-K_{\mathrm{v}}^{*}\frac{\mathbf{\Phi}_d(\mathbf{u}-\mathbf{u}_{\mathrm{s}})}{U}\left(\frac{\rho U^2}{L}\right), \tag{4}$$

where K_{v}^{*} is the feedback gain (nondimensional), U is the characteristic velocity, L is the characteristic length, and $\mathbf{u}_{\mathrm{s}}$ is the velocity vector of the real blood flow. $\mathbf{\Phi}_d$ $(d=1,\ 2,\ 3)$ is a projection function of a three-dimensional vector to the d-dimensional subspace [21]. The projection of the three-dimensional velocity vector in the direction of the ultrasonic beam in the UMI simulation corresponds to the case of $d=1$, and $\mathbf{\Phi}_1(\mathbf{u})$ and $\mathbf{\Phi}_1(\mathbf{u}_{\mathrm{s}})$ correspond to computed and measured Doppler velocities, respectively. Here, measurement errors, such as noise, contained in ultrasonic Doppler measurement are ignored for simplicity. Note that, in our previous study [23], the effects of major measurement errors on the computational accuracy of the UMI simulation were investigated, and methods to compensate those effects were proposed. The special case with $K_{\mathrm{v}}^{*}=0$ corresponds to the ordinary numerical simulation without feedback.

Previous studies [21–23] have revealed that with a proper application of feedback, the computational velocity field approaches the real velocity field of the blood flow. Generally, because a velocity field has a unique pressure field, it was expected that the computational pressure field would concurrently approach the real pressure field. However, the reproducibility of pressure field was not necessarily satisfactory.

The pressure field by the UMI simulation is discussed in the following. The velocity field, $\mathbf{u}_{\mathrm{s}}$, and the pressure field, p_{s}, of a real blood flow satisfy governing Equations (1) and (3) without the external force term, $\mathbf{f}$, with the upstream and downstream boundary conditions of the correct velocity profiles and with the initial condition of the correct velocity vector field at the first time step:

$$\rho\left(\frac{\partial \mathbf{u}_{\mathrm{s}}}{\partial t}+(\mathbf{u}_{\mathrm{s}}\cdot\nabla)\,\mathbf{u}_{\mathrm{s}}\right)=\mu\Delta\mathbf{u}_{\mathrm{s}}-\nabla p_{\mathrm{s}}, \tag{5}$$

$$\Delta p_{\mathrm{s}}=-\nabla\cdot\rho(\mathbf{u}_{\mathrm{s}}\cdot\nabla)\,\mathbf{u}_{\mathrm{s}}. \tag{6}$$

DOI: 10.1002/cnm

In the UMI simulation, incorrect specification of boundary conditions introduces error to the computational result as compared with the real blood flow, but the feedback based on Doppler velocity works to reduce the error in the velocity vector field in the feedback domain. Therefore, in the equation derived from the subtraction of Equation (6) from Equation (3), the velocity vector, $\mathbf{u}$, is approximately equal to the real velocity vector, $\mathbf{u}_s$, and the following equation is approximately satisfied in the feedback domain:

$$\Delta p = \Delta p_s + \nabla \cdot \mathbf{f}. \tag{7}$$

This equation implies that the pressure field, p, of the UMI simulation becomes different from the real pressure field, p_s, because of the effect of feedback in the case that the divergence of the feedback force vector is not zero.

2.2. *Pressure compensation method*

A pressure compensation method for the UMI simulation is introduced. The pressure compensation is applied after the convergent results of velocity and pressure are obtained (see Figure 1). The correct pressure field, p_s, is expressed as the summation of the computational result, p, and the compensation term, p_f.

$$p_s = p + p_f. \tag{8}$$

With Equation (7) and Equation (8) operated by Laplacian operator, the following equation is obtained.

$$\Delta p_f = -\nabla \cdot \mathbf{f}. \tag{9}$$

The pressure compensation, p_f, is calculated from Equation (9) by setting zero value at the boundaries of the computation domain. In the case that the blood flow is considered to be parallel flow such as the one in a straight blood vessel, pressure is constant over the cross-section perpendicular to the flow. In addition, if the flow rate in the UMI simulation is identical to that of the real flow, the pressure differences between upstream and downstream boundaries are the same between the cases. Consequently, the boundary conditions of the pressure equations for p and p_s can be considered to be the same. Because $p_f = p_s - p$ from Equation (8), the value of p_f should be zero at the upstream and downstream boundaries. By substituting the pressure compensation, p_f, into Equation (8), an estimated value, p'_s, of the correct pressure is obtained.

The proposed pressure compensation method is equivalent to a modification of the UMI simulation retaining only the divergence-free part of the feedback signal, $\mathbf{f}_{div}$. The feedback signal, $\mathbf{f}$, can be decomposed to an irrotational part, $\mathbf{f}_{irr}$, and a divergence-free part, based on Helmholtz decomposition [25]. Pressure compensation, p_f, obtained from Equation (9) determines the irrotational part of the feedback signal as $\mathbf{f}_{irr} = -\nabla p_f$, which does not contribute to improvement of the computational accuracy of the velocity field, but deteriorates that of the pressure field.

2.3. *Discretization*

Outlines of discretization of the governing equations of the UMI simulation, including the pressure compensation equation, are described in this section. The above-mentioned governing equations are discretized by means of the finite volume method and are solved with the SIMPLER method [26]. The concrete notations of the parameters in the following equations, and supplementary pressure correction equations and velocity correction procedure in the SIMPLER method, are explained in [26].

The x-directional momentum equation in Navier–Stokes equations of Equation (1):

$$B_p u_{i,j,k} = \sum B_{nb} u_{nb} + S_{i,j,k} + A_i (p_{i-1,j,k} - p_{i,j,k}) + \Delta V_{i,j,k} f_{x_{i,j,k}}, \tag{10}$$

where Bs are the elements of the matrix consisting of all of the diffusive terms and a part of the convective terms in the discretized Navier–Stokes equation, and $(\sum B_{nb} u_{nb})$ is the summation of

DOI: 10.1002/cnm

the values at six adjacent nodes in the three-dimensional computation. The second term, $S_{i,j,k}$, on the right side is the source term, which consists of a part of the convective terms and a part of the time-derivative term. The third term is the pressure gradient term in which A_i is the cross-sectional area of the control volume, and the last term is the feedback term in which $\Delta V_{i,j,k}$ is the volume of the cell. Subscript p denotes the position where $u(i,\ j,\ k)$ is defined, and *nb* means adjacent nodes. Equations for y-directional and z-directional momentums are analogous to that in Equation (10).

The pressure equation of Equation (3):

$$C_P p_{i,j,k} = \sum C_{nb} p_{nb} + S_{p_{i,j,k}} + S_{f_{i,j,k}}, \tag{11}$$

where Cs are the elements of the matrix derived from discretization of the pressure equation, $S_{pi,j,k}$ is the source term derived from discretization of the first term on the right side of Equation (3), and $S_{fi,j,k}$ is the source term because of the feedback. Subscript P denotes the position where $p(i,\ j,\ k)$ is defined. The source term because of the feedback, $S_{fi,j,k}$, is denoted in the following equation:

$$S_{f_{i,j,k}} = \frac{\rho}{B_p}[(f_{x\,i,j,k} - f_{x\,i+1,j,k})A_i + (f_{y\,i,j,k} - f_{y\,i,j+1,k})\,A_j + (f_{z\,i,j,k} - f_{z\,i,j,k+1})A_k], \tag{12}$$

where A_i, A_j, and A_k are the cross-sectional areas of the control volume facing each direction.

Pressure compensation for feedback of Equation (9):

Equation (9) is also expressed in a way similar to the pressure equation

$$C_p p_{f_{i,j,k}} = \sum C_{nb} p_{f_{nb}} - S_{f_{i,j,k}}, \tag{13}$$

where coefficients C_p and C_{nb}, and the source term $S_{fi,j,k}$ are identical with those in Equations (11) and (12).

3. VALIDATION WITH NUMERICAL EXPERIMENT

Results of the theoretical analysis and the proposed pressure compensation method are validated by a numerical experiment dealing with a synthetic three-dimensional steady flow in a thoracic aneurysm. Ultrasonic measurement provides the Doppler velocity necessary for the feedback in UMI simulation, but it does not provide other information necessary for evaluating the UMI simulation such as three-dimensional velocity vectors or pressure field. Hence, we do not use real measurement data for the reference data. Instead, we use a numerical solution for a synthetic steady flow with realistic upstream and downstream velocity boundary conditions called 'standard solution' as a model of real blood flow to perform the numerical experiment. The boundary conditions of the standard solution are determined from a preliminary simulation of blood flow in a whole aorta including an aneurysm. Reproduction of the standard solution by the UMI simulations with/without the pressure compensation and the ordinary numerical simulation without feedback are investigated. The numerical simulations conducted in this section are summarized in Table I.

Table I. Classification of preliminary simulation (PS), standard solution (SS), UMI simulation (UMIS), and ordinary simulation (OS).

Name	Solver	Domain	Grid	Boundary velocity	Feedback	Note
PS	FLUENT	Whole aorta Figure 2(a)	Hexahedral 142,417	Uniform inlet Free stream outlet	N/A	Boundary velocity for SS was obtained.
SS	Original (SIMPLER)	Aneurysm Figure 2(b)	Orthogonal $40 \times 34 \times 49$	Specified velocity inlet & outlet	N/A	Model of real flow
UMIS	Original (SIMPLER)	Aneurysm Figure 2(b)	Orthogonal $40 \times 34 \times 49$	Uniform inlet Free stream outlet	Applied	Measurement data was was generated by SS.
OS	Original (SIMPLER)	Aneurysm Figure 2(b)	Orthogonal $40 \times 34 \times 49$	Uniform inlet Free stream outlet	N/A	

DOI: 10.1002/cnm

3.1. Methods

A numerical experiment was conducted to investigate the computational accuracy of the pressure field by the UMI simulation and to examine the efficiency of the proposed pressure compensation method. The objective was a steady flow in a thoracic aneurysm, which was the same as in a previous study [22]. A steady numerical solution with realistic boundary conditions was first defined as the standard solution. The boundary conditions of the standard solution were determined from a preliminary simulation of blood flow in a whole aorta including the aneurysm. Although generation of synthetic measurement data for validation of new algorithms has been investigated [27, 28], the computational three-dimensional velocity vectors were simply projected in the direction of the ultrasonic beam without consideration of measurement errors to obtain the Doppler velocity of the standard solution. Then, with inaccurate boundary conditions but with the correct flow volume, UMI simulation and an ordinary simulation without feedback were performed. In the UMI simulation, Doppler velocities of the standard solution were used for feedback. After the convergent results of velocity and pressure were obtained, the pressure compensation was applied to the pressure field (see Figure 1).

A preliminary simulation for a whole aorta was first performed. The configuration of the whole aorta from the ascending aorta to the abdominal aorta, including an aneurysm in the descending aorta, was reconstructed, as shown in Figure 2(a), by accumulating X-ray CT images (Aquilion 16, Toshiba, Tokyo, Japan) of a 76-year-old female patient with commercial three-dimensional reconstruction software (Mimics 7.3, Materialise, Leuven, Belgium) [22]. A preliminary simulation of a steady blood flow in the whole aorta (Figure 2(a)) was carried out by using commercial computational fluid dynamics software (FLUENT 6.1.22, Fluent, Inc., Lebanon, NH). The computational grid used in the preliminary FLUENT simulation consisted of 142,417 hexahedral elements. Pressure–velocity coupling was accomplished by the SIMPLE method, and spatial discretization schemes were employed as follows: a Green-Gauss cell-based scheme for gradient; a standard scheme for pressure; and a first-order upwind for momentum. Uniform velocity was applied at the inlet boundary so that the average flow rate became 8.65×10^{-5} m^3/s, and a

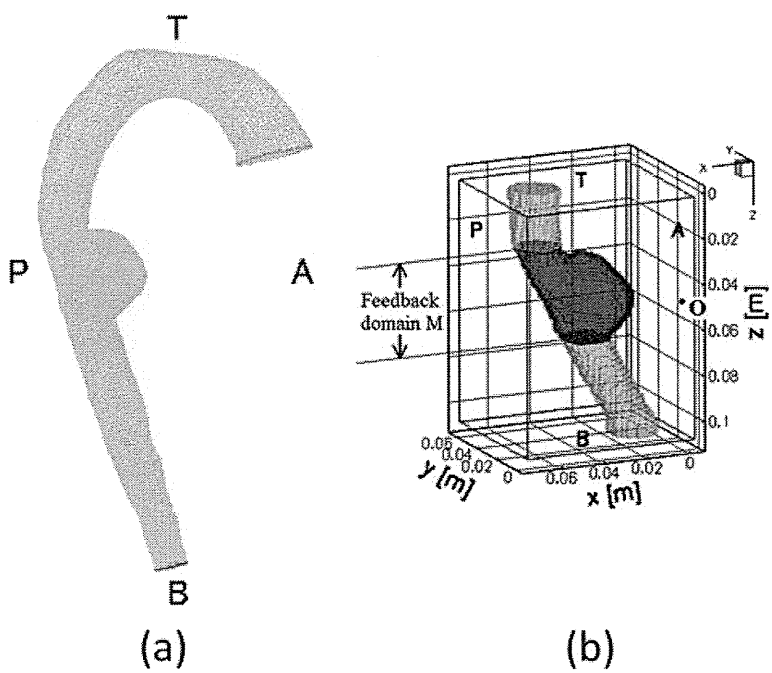

Figure 2. Computational grids for (a) a preliminary simulation of a steady flow in the whole aorta with an aneurysm in the descending aorta by using FLUENT, and for (b) the other simulations of the flow in the partial domain including the aneurysm with a feedback domain (dark gray zone) and a probe position at O.

DOI: 10.1002/cnm

free-flow condition was applied at the downstream boundary. A no-slip condition was set on the wall. The convergence criterion in the numerical simulation was set at 1×10^{-4} for momentum and continuity equations.

In the following computations for the standard solution, the UMI simulation, and the ordinary simulation, the computational domain was limited to the vicinity of the thoracic aneurysm, as shown in Figure 2(b). A computational grid system was generated by introducing a staggered grid system of $40 \times 34 \times 49$ grid points in x, y, and z directions, compromising reproducibility of vessel configuration and computational load. The grid interval dz in the z direction was set at 2.00×10^{-3} m, which was the same as the slice interval of the X-ray CT, and those in the other directions were determined to be $dx = dy = 1.78 \times 10^{-3}$ m. The equivalent diameter of the blood vessel, D, at the upstream boundary calculated by averaging x-directional and y-directional maximum lengths of the cross-section of the blood vessel at the upstream boundary was 23.47×10^{-3} m. Flow rate was set at 8.65×10^{-5} m^3/s (same as the preliminary simulation), and the average flow velocity at the upstream boundary, U, was 2.00×10^{-1} m/s. The density, ρ, and viscosity, μ, of the blood were assumed to be 1.00×10^3 kg/m^{3}and 4.00×10^{-3} Pa $\cdot$ s, respectively. All the variables were nondimensionalized with the equivalent diameter of the blood vessel, D, as the characteristic length, L, the average flow velocity as the characteristic velocity, U, and the density of blood, ρ, as the characteristic density. The Reynolds number of the steady flow was 1174. From here on, the same symbols are used for both dimensional and nondimensional values because it does not cause any confusion.

In the computation of the standard solution, velocity profiles at the upstream and downstream boundaries were determined as those on the corresponding cross-sections of the preliminary simulation. In the UMI simulation and the ordinary simulation, a uniform parallel flow was applied at the upstream boundary, and the free flow condition was set at the downstream boundary.

Because the computational result converges to the target flow with the aid of the feedback process, unsteady flow computation is required for the UMI simulation even for the present steady target flow. Time-dependent computation was performed for all cases. The computational time increment was set as $\Delta t = 0.01(1.17 \times 10^{-3}$ s) [22].

In UMI simulation, considering the acquisition of Doppler velocities in the three-dimensional domain by transesophageal ultrasonography, the ultrasound probe or the origin of ultrasonic beam was set at $O[(x, y, z) = (0.008, 0.023, 2.045)((0.000$ m, 0.001 m, 0.048 m))], which was located at the same height as the aneurysm, as shown in Figure 2(b). The Doppler beam direction was along a line from the origin of ultrasonic beam to each computational gird point. Blood flow in the whole aneurysmal domain $M[1.193 \leqslant z \leqslant 2.897(0.028$ m $\leqslant z \leqslant 0.068$ m), shown by a dark gray zone in Figure 2(b)], including the parent blood vessel, was assumed to be measured. Domain M was defined as the feedback domain, and at all the grid points in the fluid region of domain M, feedback signals were added to the UMI simulation based on the differences of Doppler velocities between the simulation and the standard solution.

In the computation of the standard solution, the UMI simulation and the ordinary simulation, the governing equations were discretized by the finite volume method and were solved with an original program based on the SIMPLER method [26, 29] as described in the previous section. The convective terms were discretized with the reformulated QUICK scheme [30], and the time derivative terms were discretized with the first Euler implicit scheme. Linear algebraic equations were solved using the modified strongly implicit (MSI) scheme [31]. The convergence criterion in the numerical simulation was set at 1×10^{-4} for momentum and continuity equations.

To evaluate the computational accuracy of the UMI simulation and the ordinary simulation, a space-averaged error norm of a variable, a (velocity vector, $\mathbf{u}$, or pressure, p), in a monitoring domain Ω was defined by the following equation:

$$\bar{e}_{\Omega}(a,t) = \frac{1}{N} \sum_{X_n \in \Omega} \left| \frac{a_{cn}(t) - a_{sn}(t)}{a_{\mathrm{ref}}} \right|, \tag{14}$$

where n and N are the identification number and the total number of the monitoring points, respectively, $|\cdot|$ is the absolute value for scalar variables or the l_1 norm, $|u| + |v| + |w|$, for velocity vector $\mathbf{u}$, and a_{ref} is the characteristic value for normalization: $a_{\mathrm{ref}} = U$ for velocity or $a_{\mathrm{ref}} = \rho U^2$

DOI: 10.1002/cnm

for pressure. Subscripts, c and s, means UMI simulation or ordinary simulation and the standard solution, respectively.

3.2. *Results and discussion*

The results of the UMI simulation with/without pressure compensation were evaluated by error norms of the velocity vector and pressure in feedback domain M (or the aneurysmal domain), $\bar{e}_{\mathrm{M}}(\mathbf{u},\ t)$ and $\bar{e}_{\mathrm{M}}(p,\ t)$, and compared with those of the ordinary numerical simulation. The variations of $\bar{e}_{\mathrm{M}}(\mathbf{u},\ t)$ and $\bar{e}_{\mathrm{M}}(p,\ t)$ of the UMI simulations at $K_{\mathrm{v}}^{*} = 0$, 80 and 160 are shown in Figure 3. The UMI simulations diverge at $K_{\mathrm{v}}^{*} \geqslant 170$ in the case of $\Delta t = 0.01$ as revealed in our previous study [22]. There is an inversely proportional relationship between the time increment and the maximum feedback gain. Concerning this issue, we theoretically clarified that the feedback signal in the source term destabilized the iterative calculation, and proposed a computational scheme to remove the destabilization phenomenon [32]. However, we used the previous scheme in this study because improvement of computational accuracy of pressure can be discussed in a stable region with the feedback gain of $K_{\mathrm{v}}^{*} < 170$. In the case of $K_{\mathrm{v}}^{*} = 0$, which corresponds to the ordinary simulation without feedback, neither error norm temporally changes because the steady solution was set as the initial condition (a dotted line in Figure 3). In contrast, by applying feedback in the UMI simulations at $K_{\mathrm{v}}^{*} = 80$ and 160, the error norm of the velocity vector, $\bar{e}_{\mathrm{M}}(\mathbf{u},\ t)$, monotonically decreases and converges at each constant value (dashed and solid black lines in Figure 3(a)). This indicates that the velocity field of the UMI simulation is closer to the standard solution than that of the ordinary

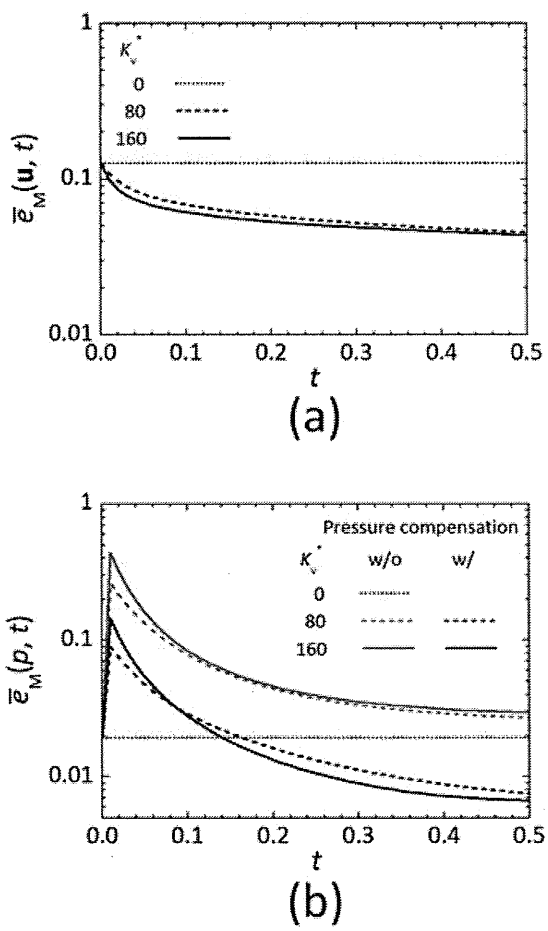

Figure 3. Transient changes of space-averaged error norms of (a) velocity vector and (b) pressure in the feedback domain in the UMI simulations without/with pressure compensation at $K_{\mathrm{v}}^{*} = 0$, 80, and 160 (nondimensional).

DOI: 10.1002/cnm

simulation. Moreover, the larger feedback gain reduces the error more rapidly. On the other hand, the error norm of pressure, $\bar{e}_{\mathrm{M}}(p,\ t)$, of the UMI simulations without pressure compensation drastically increases at the first time step ($t = 0.01$), and then decreases toward each constant value (dashed and solid gray lines in Figure 3(b)). With either feedback gain, the convergent value of $\bar{e}_{\mathrm{M}}(p,\ t)$ remains larger than that of the ordinary simulation, indicating deterioration of the computational accuracy of the pressure field by the feedback. Generally, improvement of the computational accuracy of the velocity field leads to better reproduction of the pressure field as time progresses. However, as described in the theoretical analysis, pressure error against the standard solution arises because the feedback signals do not become zero so as to reduce the error derived from a constant difference of the boundary conditions. The results of $\bar{e}_{\mathrm{M}}(p,\ t)$ by the UMI simulations at $K_{\mathrm{v}}^{*} = 80$ and 160 with pressure compensation are presented with dashed and solid black lines in Figure 3(b), respectively. In the time of $t > 0.2$, the error norms of the pressure of the UMI simulations are smaller than that of the ordinary simulation. This means that the pressure field approaches the standard solution, cancelling the error in the pressure field caused by feedback signals. Moreover, the UMI simulation with a large feedback gain $\left(K_{\mathrm{v}}^{*} = 160\right)$ presents a larger value of $\bar{e}_{\mathrm{M}}(p,\ t)$ than that of the UMI simulation with a small feedback gain $\left(K_{\mathrm{v}}^{*} = 80\right)$ at the beginning of the computation, but it finally gives a smaller convergent value.

The variations of steady values of the space-averaged error norms of the velocity vector and pressure in the feedback domain M, $\bar{e}_{\mathrm{M}}(\mathbf{u},\ t_{\infty})$ and $\bar{e}_{\mathrm{M}}(p,\ t_{\infty})$ ($t_{\infty} = 20$), with the feedback gain are shown in Figure 4. In the UMI simulation, the value of $\bar{e}_{\mathrm{M}}(\mathbf{u},\ t_{\infty})$ monotonically decreases

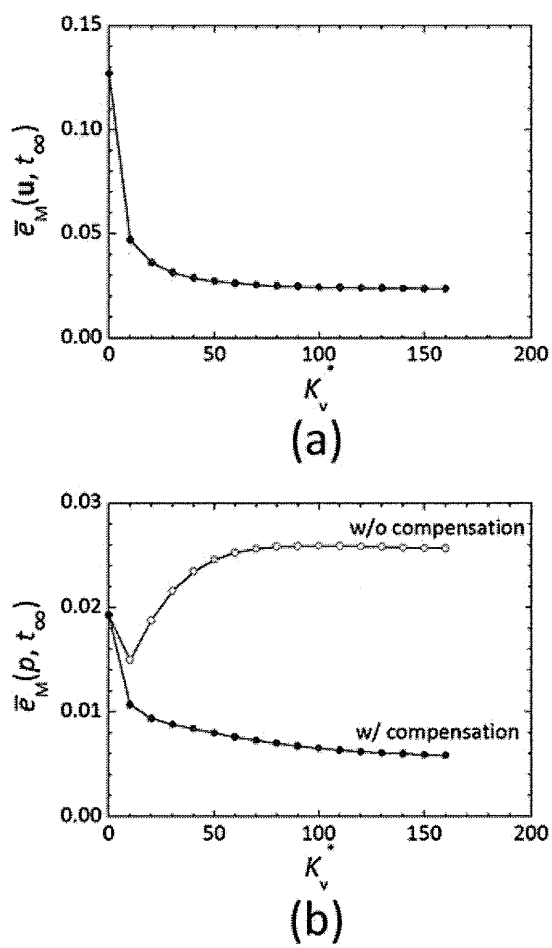

Figure 4. Variations of steady values of space-averaged error norms of (a) velocity vector and (b) pressure in the feedback domain with feedback gain (nondimensional).

DOI: 10.1002/cnm

with increasing feedback gain (Figure 4(a)). Note that the error norm of the velocity vector in the UMI simulation is not affected by the pressure compensation. However, the value of $\bar{e}_{\mathrm{M}}(p,\ t_\infty)$ at first decreases and then increases (open circle plots in Figure 4(b)). In $K_{\mathrm{v}}^* > 20$, the error norm is larger than that of the ordinary simulation $\left(K_{\mathrm{v}}^* = 0\right)$. When the feedback gain is relatively small $\left(K_{\mathrm{v}}^* < 20\right)$, the computational accuracy of the pressure field seems to be improved in accordance with the improvement of that of the velocity field because the pressure deviation as a result of the application of artificial body forces (or feedback signals) is not significant. With large feedback gain, however, the ability to reproduce the pressure field deteriorates because the significant artificial body forces proportional to the feedback gain are applied. In contrast, as the feedback gain increases, the value of $\bar{e}_{\mathrm{M}}(p,\ t_\infty)$ after the pressure compensation monotonically decreases, similar to that of the velocity vectors (solid circle plots in Figure 4(b)). This reflects the fact that the pressure field concurrently becomes closer to the standard solution with the velocity field. Regarding the determination of the feedback gain, K_{v}^*, in the practical application of the UMI simulation, although the UMI simulation with a large feedback gain reduces the error against the measurement data, it reproduces the measurement error as well. In our previous study [23], the effects of major measurement errors on the computational accuracy of the UMI simulation were investigated, and methods to compensate those effects were proposed. An appropriate value of the feedback gain should be determined based on the results, considering how much compensation is achieved. It is also noted that the UMI simulation has sufficiently high frequency response characteristics to ensure the convergence to the unsteady flow [22].

The result of the UMI simulation at $K_{\mathrm{v}}^* = 160$ is further investigated in the following. The steady values of the space-averaged error norms of velocity vector and pressure against the standard solution in each z-directional cross-section, $\bar{e}_{\mathrm{cs}(z)}(\mathbf{u},\ t_\infty)$ and $\bar{e}_{\mathrm{cs}(z)}(p,\ t_\infty)$ $(t_\infty = 20)$, in the ordinary simulation $\left(K_{\mathrm{v}}^* = 0\right)$ and the UMI simulations without/with the pressure compensation are shown in Figure 5(a) and (b), respectively. The dotted line and the gray and black solid lines represent the results of the ordinary simulation and the UMI simulations without and with the pressure compensation, respectively, and the gray area indicates the feedback domain in the UMI simulation. Compared with the ordinary simulation, in the case of the UMI simulations, the error norm of the velocity vector, $\bar{e}_{\mathrm{cs}(z)}(\mathbf{u},\ t_\infty)$, is decreased after the feedback domain $(z \geqslant 1.193)$, and remains smaller in a certain downstream region of the feedback domain $(2.897 < z < 3.8)$, as shown by the solid lines in Figure 5(a). Regarding the error norm of pressure, $\bar{e}_{\mathrm{cs}(z)}(p,\ t_\infty)$, shown in Figure 5(b), the UMI simulation with the pressure compensation presented a smaller value than the ordinary simulation in all z-directional cross-sections and almost the same value near the downstream boundary, implying the ability to reproduce the pressure field with good accuracy. On the other hand, the error norm of pressure, $\bar{e}_{\mathrm{cs}(z)}(p,\ t_\infty)$, in the UMI simulation without pressure compensation increases in the upstream region of the feedback domain and exceeds that of the ordinary simulation with the peak value near the upstream boundary of the feedback domain. It then decreases in the downstream direction and becomes the same as that in the UMI simulation with the pressure compensation. Figure 5(c) shows a summation of absolute values of the divergence of the feedback force vector in each z-directional cross-section. The value is large in the upstream side in the feedback domain where the error in the velocity field is large, especially at the upstream boundary of the feedback domain where feedback signals discontinuously change. Moreover, in comparison with Figure 5(b), the large value of the divergence of the feedback force vector also influences the computational accuracy of the pressure field in the upstream domain before the feedback domain where the divergence is zero.

The pressure distributions on a y-directional cross-section $(y = 1.462)$ of the standard solution, the ordinary simulation $\left(K_{\mathrm{v}}^* = 0\right)$, and the UMI simulations $\left(K_{\mathrm{v}}^* = 160\right)$ without/with the pressure compensation are depicted in Figure 6. Between the pressure fields of the standard solution and the ordinary simulation, p_{s} and p_{o} (Figures 6(a) and (b)), a difference can be observed near the upstream boundary, but similar pressure profiles are obtained in the aneurysm. As observed in the error norm of pressure in Figure 5(b), the UMI simulation without pressure compensation (Figure 6(c)) provides a pressure distribution different from that of the standard solution (Figure 6(a)), especially in the upstream region of the feedback domain (see an arrow), but it gives almost the same distribution in the aneurysm. In the UMI simulation with the pressure compensation (Figure 6(d)),

DOI: 10.1002/cnm

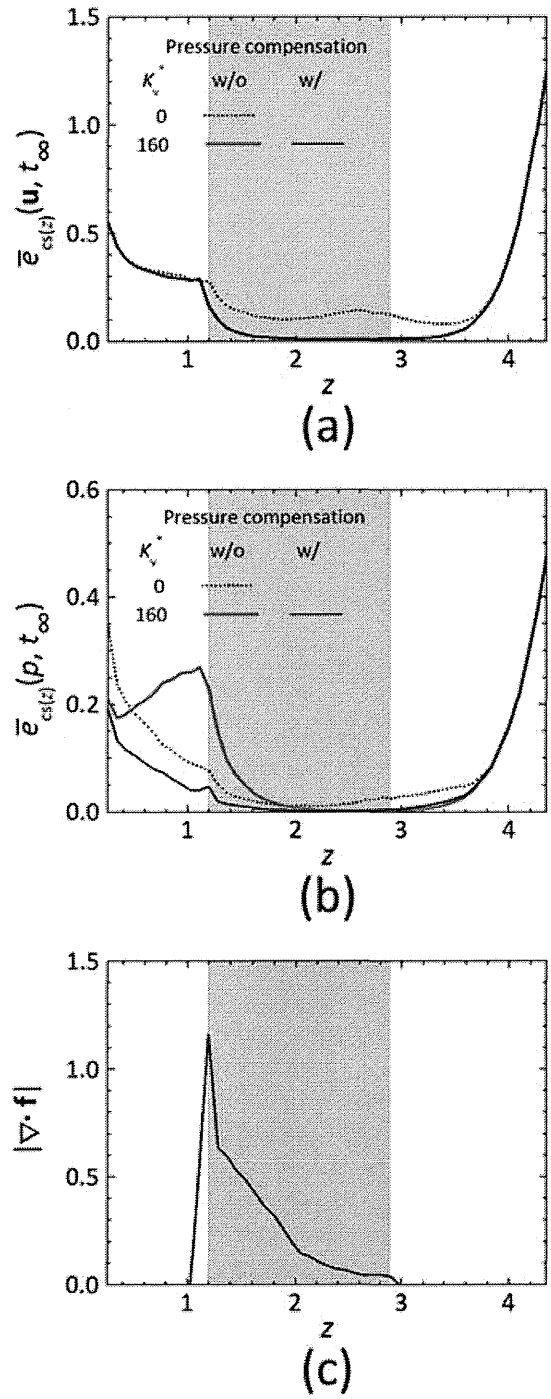

Figure 5. Steady values of space-averaged error norms of (a) velocity vector and (b) pressure, and (c) space-averaged absolute value of divergence of feedback signal vector in each z-directional cross-section (nondimensional). The gray zone implies the feedback domain.

the difference in pressure distribution observed in the UMI simulation without the pressure compensation is properly improved.

The distributions of error norm of pressure against the standard solution on the corresponding y-directional cross-section are shown in Figure 7. As mentioned above, the ordinary simulation and the UMI simulation without the pressure compensation show relatively large error near the upstream

DOI: 10.1002/cnm

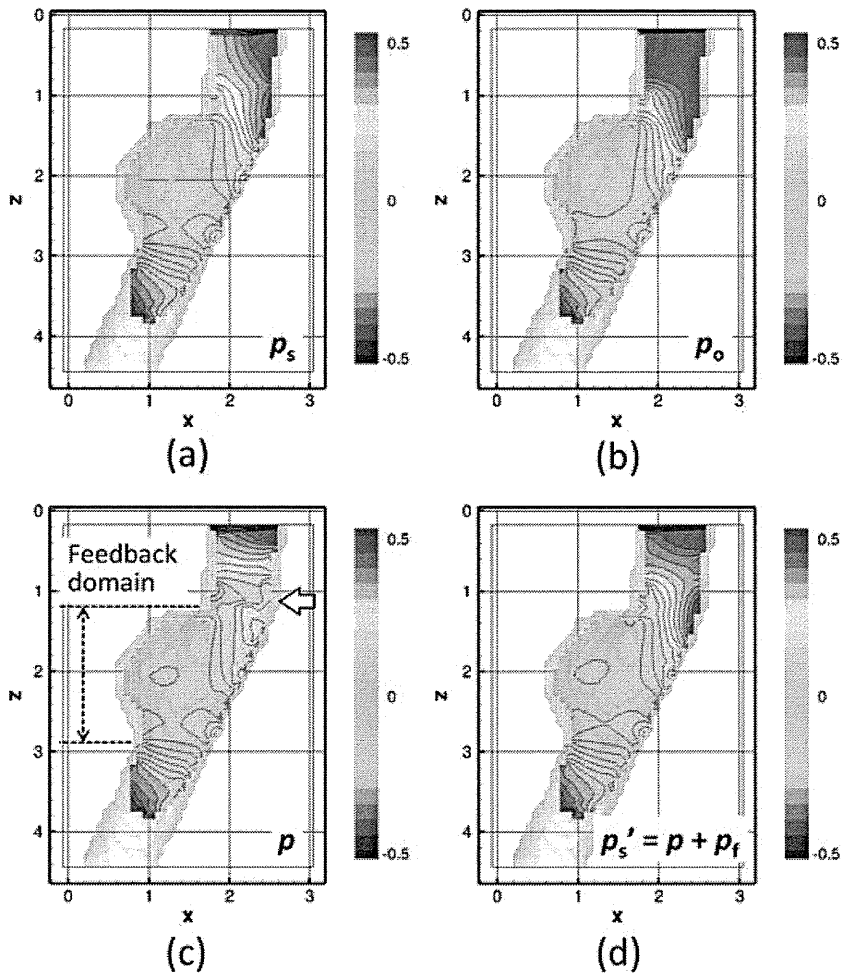

Figure 6. Pressure distribution on a y-directional cross-section ($y = 1.462$): (a) standard solution, p_s, (b) ordinary simulation $\left(K_v^* = 0\right)$, p_o, and UMI simulations (c) without and (d) with pressure compensation at $K_v^* = 160$, p and p_s', respectively (nondimensional).

boundary and in the vicinity of the upstream boundary of the feedback domain, respectively. In contrast, the error in the UMI simulation with the pressure compensation is relatively small in the whole domain.

The distribution of the divergence of the feedback force vector in the UMI simulation is demonstrated in Figure 8(a). There is a region with a large magnitude of divergence of the feedback force vector near the upstream boundary of the feedback domain. Figure 8(b) shows the distribution of the pressure compensation in the UMI simulation, p_f, calculated from Equation (9). It is noted that the distribution of the pressure compensation has a pattern similar to that of the error norm of the pressure for the UMI simulation without the pressure compensation in Figure 7(b). By adding the pressure compensation, p_f (Figure 8(b)), to the result of the UMI simulation without compensation (Figure 6(c)), a compensated pressure field, p_s' (Figure 6(d)), is obtained.

In summary, the numerical experiment dealing with a three-dimensional steady flow in a thoracic aneurysm indicates that feedback signals in the UMI simulation can deteriorate the reproducibility of the pressure field, while improving that of the velocity field. However, by properly compensating the effects of the feedback signals on the pressure with the proposed method, both the velocity and pressure fields of the standard solution can be properly reproduced.

DOI: 10.1002/cnm

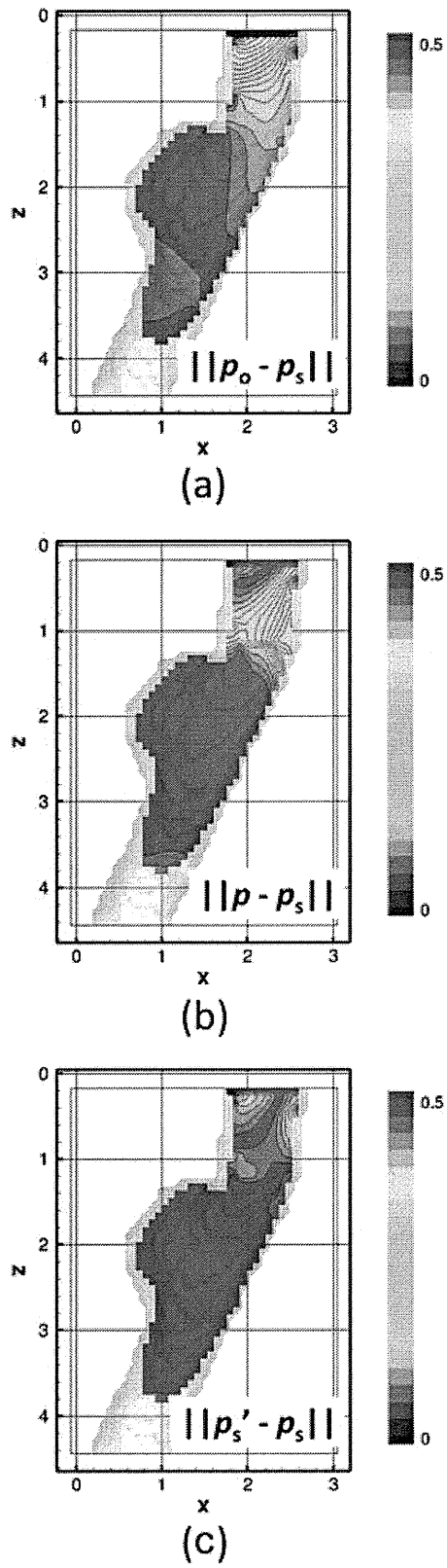

Figure 7. Error norm of pressure on a y-directional cross-section ($y = 1.462$): (a) ordinary numerical simulation $\left(K_v^* = 0\right)$, and UMI simulations (b) without and (c) with pressure compensation at $K_v^* = 160$, respectively (nondimensional).

DOI: 10.1002/cnm

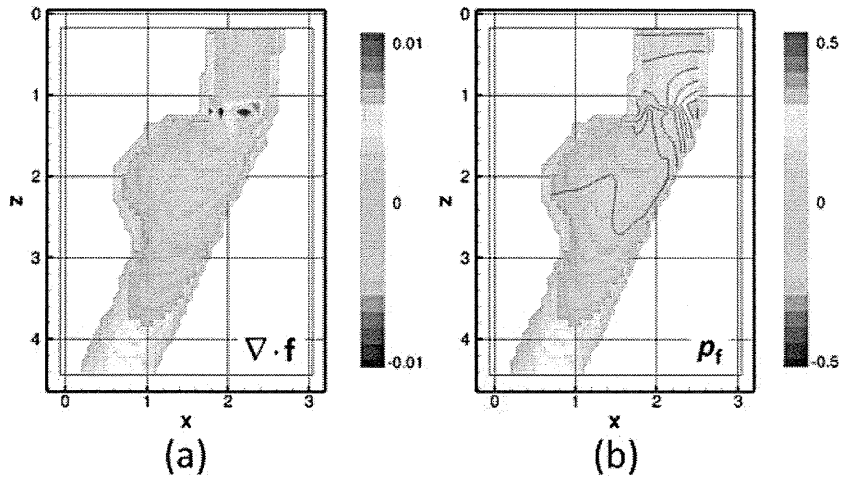

Figure 8. Distributions of (a) divergence of feedback force vector and (b) value for pressure compensation, p_f, in the UMI simulation at $K_v^* = 160$ (nondimensional).

4. CONCLUSION

In this study, reproduction of the pressure field by UMI simulation was investigated. The effect of feedback based on Doppler velocity on the pressure field was first examined by theoretical analysis. When the divergence of the feedback force vector was not zero, it influenced the pressure field in the UMI simulation, while improving the computational accuracy of the velocity field. Hence, a method to estimate the correct pressure by compensating the pressure field was devised. A numerical experiment was conducted dealing with the reproduction of a three-dimensional steady flow in a thoracic aneurysm to validate results of the theoretical analysis. The ability of the UMI simulation to reproduce the pressure field deteriorated with a large feedback gain. However, by properly compensating the effects of the feedback signals on the pressure, the error in the pressure field was reduced, exhibiting improvement of the computational accuracy in comparison with that of the ordinary simulation. Hence, the UMI simulation with pressure compensation allows for the reproduction of both velocity and pressure fields of blood flow. The information on hemodynamic stresses (wall shear stress and pressure) and blood flow dynamics enables a better understanding of blood flow and would provide novel indices for diagnosis of diseases. To perform the UMI simulation in a clinical setting, further investigations on automatic excursion of the sequential computation including reconstruction of the blood vessel configuration and recognitions of the position and orientation of the ultrasound probe are required.

REFERENCES

1. Friedman MH, Krams R, Chandran KB. Flow interactions with cells and tissues: cardiovascular flows and fluid-structure interactions. *Annals of Biomedical Engineering* 2010; **38**:1178–1187.
2. Taylor CA, Steinman DA. Image-based modeling of blood flow and vessel wall dynamics: applications, methods and future directions. *Annals of Biomedical Engineering* 2010; **38**:1188–1203.
3. Morris L, Delassus P, Grace P, Wallis F, Walsh M, McGloughlin T. Effects of flat, parabolic and realistic steady flow inlet profiles on idealised and realistic stent graft fits through Abdominal Aortic Aneurysms (AAA). *Medical Engineering & Physics* 2006; **28**:19–26.
4. Moyle KR, Antiga L, Steinman DA. Inlet conditions for image-based CFD models of the carotid bifurcation: is it reasonable to assume fully developed flow? *Journal of Biomechanical Engineering-Transactions of the ASME* 2006; **128**:371–379.
5. Formaggia L, Gerbeau JF, Nobile F, Quarteroni A. Numerical treatment of defective boundary conditions for the Navier-Stokes equations. *SIAM Journal on Numerical Analysis* 2002; **40**:376–401.
6. Veneziani A, Vergara C. An approximate method for solving incompressible Navier-Stokes problems with flow rate conditions. *Computer Methods in Applied Mechanics and Engineering* 2007; **196**:1685–1700.

DOI: 10.1002/cnm

7. McGregor RH, Szczerba D, von Siebenthal M, Muralidhar K, Szekely G. Exploring the use of proper orthogonal decomposition for enhancing blood flow images via computational fluid dynamics. *Medical Image Computing and Computer Assisted Intervention* 2008; **11**:782–789.
8. McGregor RH, Szczerbal D, Muralidhar K, Szekely G. A fast alternative to computational fluid dynamics for high quality imaging of blood flow. *Medical Image Computing and Computer Assisted Intervention* 2009; **12**:124–131.
9. Zeldin BA, Meade AJ. Integrating experimental data and mathematical models in simulation of physical systems. *AIAA Journal* 1997; **35**:1787–1790.
10. Dwight RP. Bayesian inference for data assimilation using least-squares finite element methods. *IOP Conference Series: Materials Science and Engineering* 2010; **10**:012224.
11. Heys JJ, Manteuffel TA, McCormick SF, Milano M, Westerdale J, Belohlavek M. Weighted least-squares finite elements based on particle imaging velocimetry data. *Journal of Computational Physics* 2010; **229**:107–118.
12. Bertoglio C, Moireau P, Gerbeau JF. Sequential parameter estimation for fluid-structure problems. Application to hemodynamics. *International Journal for Numerical Methods in Biomedical Engineering* 2012; **28**:434–455.
13. D'Elia M, Perego M, Veneziani A. A variational data assimilation procedure for the incompressible Navier-Stokes equations in hemodynamics. *Journal of Scientific Computing* 2012; **52**:340–359.
14. Munro R, Kopken C, Kelly G, Thepaut JN, Saunders R. Assimilation of Meteosat radiance data within the 4D-Var system at ECMWF: data quality monitoring, bias correction and single-cycle experiments. *Quarterly Journal of the Royal Meteorological Society* 2004; **130**:2293–2313.
15. Hayase T, Hayashi S. State estimator of flow as an integrated computational method with the feedback of online experimental measurement. *Journal of Fluids Engineering-Transactions of the ASME* 1997; **119**:814–822.
16. Nisugi K, Hayase T, Shirai A. Fundamental study of hybrid wind tunnel integrating numerical simulation and experiment in analysis of flow field. *JSME International Journal Series B-Fluids and Thermal Engineering* 2004; **47**:593–604.
17. Yamagata T, Hayase T, Higuchi H. Effect of feedback data rate in PIV measurement-integrated simulation. *Journal of Fluid Science and Technology* 2008; **3**:477–487.
18. Nakao M, Kawashima K, Kagawa T. Application of MI simulation using a turbulent model for unsteady orifice flow. *Journal of Fluids Engineering-Transactions of the ASME* 2009; **131**:111401.
19. Funamoto K, Hayase T, Shirai A, Saijo Y, Yambe T. Fundamental study of ultrasonic-measurement-integrated simulation of real blood flow in the aorta. *Annals of Biomedical Engineering* 2005; **33**:415–428.
20. Funamoto K, Suzuki Y, Hayase T, Kosugi T, Isoda H. Numerical validation of MR-measurement-integrated simulation of blood flow in a cerebral aneurysm. *Annals of Biomedical Engineering* 2009; **37**:1105–1116.
21. Funamoto K, Hayase T, Saijo Y, Yambe T. Numerical experiment for ultrasonic-measurement-integrated simulation of three-dimensional unsteady blood flow. *Annals of Biomedical Engineering* 2008; **36**:1383–1397.
22. Funamoto K, Hayase T, Saijo Y, Yambe T. Numerical experiment of transient and steady characteristics of ultrasonic-measurement-integrated simulation in three-dimensional blood flow analysis. *Annals of Biomedical Engineering* 2009; **37**:34–49.
23. Funamoto K, Hayase T, Saijo Y, Yambe T. Numerical analysis of effects of measurement errors on ultrasonic-measurement-integrated simulation. *IEEE Transactions on Biomedical Engineering* 2011; **58**:653–663.
24. Funamoto K, Hayase T, Saijo Y, Yambe T. Numerical study on variation of feedback methods in ultrasonic-measurement-integrated simulation of blood flow in the aneurysmal aorta. *JSME International Journal Series C-Mechanical Systems, Machine Elements and Manufacturing* 2006; **49**:144–155.
25. Arfken GB, Weber HJ. *Mathematical Methods for Physicists*. Elsevier Academic Press: Amsterdam/Boston/Tokyo, 2005.
26. Patankar SV. *Numerical Heat Transfer and Fluid Flow*. Hemisphere Pub. Corp.: Washington DC/New York, 1980.
27. Morbiducci U, Ponzini R, Rizzo G, Biancolini ME, Iannaccone F, Gallo D, Redaelli A. Synthetic dataset generation for the analysis and the evaluation of image-based hemodynamics of the human aorta. *Medical & Biological Engineering & Computing* 2012; **50**:145–154.
28. Swillens A, De Schryver T, Lovstakken L, Torp H, Segers P. Assessment of numerical simulation strategies for ultrasonic color blood flow imaging, based on a computer and experimental model of the carotid artery. *Annals of Biomedical Engineering* 2009; **37**:2188–2199.
29. Hayase T, Humphrey JAC, Greif R. Mini-manual for ROTFLO2. *Department of Mechanical Engineering Report*, University of California, Berkeley, 1990; FM-90-1.
30. Hayase T, Humphrey JAC, Greif R. A consistently formulated QUICK scheme for fast and stable convergence using finite-volume iterative calculation procedures. *Journal of Computational Physics* 1992; **98**:108–118.
31. Schneider GE, Zedan M. A modified strongly implicit procedure for the numerical solution of field problems. *Numerical Heat Transfer* 1981; **4**:1–19.
32. Hayase T, Imagawa K, Funamoto K, Shirai A. Stabilization of measurement-integrated simulation by elucidation of destabilizing mechanism. *Journal of Fluid Science and Technology* 2010; **5**:632–647.

DOI: 10.1002/cnm

電気学会論文誌 C（電子・情報・システム部門誌）
IEEJ Transactions on Electronics, Information and Systems
Vol.132 No.12 pp.1943–1948　DOI: 10.1541/ieejeiss.132.1943

論　文

植込み型除細動器への実装を考慮した致死性不整脈検出アルゴリズムの改良

正　員　阿部　　誠*　非会員　吉澤　　誠**　非会員　テルマ　ケイコ　スガイ***
非会員　本間　経康**　非会員　杉田　典大*　非会員　清水　一夫****
非会員　後藤　　萌****　非会員　稲垣　正司*5　非会員　杉町　　勝*5
非会員　砂川　賢二*6

Improving Detection Algorithm of Life-threatening Arrhythmias for Implementation of Implantable Cardioverter-Defibrillators

Makoto Abe*, Member, Makoto Yoshizawa**, Non-member, Telma Keiko Sugai***, Non-member, Noriyasu Homma**, Non-member, Norihiro Sugita*, Non-member, Kazuo Shimizu****, Non-member, Moe Goto****, Non-member, Masashi Inagaki*5, Non-member, Masaru Sugimachi*5, Non-member, Kenji Sunagawa*6, Non-member

（2012年2月29日受付，2012年6月28日再受付）

The implantable cardioverter-defibrillator (ICD) is an effective therapeutic device for rescuing patients with cardiac diseases from death caused by life-threatening arrhythmias. The authors previously proposed a detection algorithm of life-threatening arrhythmias with a multiple regression model. To enhance the classification accuracy, in the present study, we have introduced an autoregressive filter and a multiple detection process into the previous detection algorithm. The experimental results showed that the proposed method could attain a high accuracy such that all ventricular fibrillation rhythms could be exactly detected. In addition, detection errors of sinus rhythms or supraventricular tachyarrhythmias provoking the ICD malfunction were reduced.

キーワード：植込み型除細動器，致死性不整脈，重回帰モデル
Keywords: implantable cardioverter-defibrillator, life-threatening arrhythmia, multiple regression model

1. はじめに

日本における心血管系疾患に起因する心臓突然死による年間死者数は6万人以上といわれており，その対策は医学的かつ社会的な課題となっている(1)。心臓突然死において心臓が停止する直接の原因は，心室頻拍 (VT: Ventricular Tachycardia) や心室細動 (VF: Ventricular Fibrillation) といわれる心室性頻脈性不整脈であり，全体の80〜90%を

* 東北大学大学院工学研究科
〒980-8578　宮城県仙台市青葉区荒巻字青葉6-3
Graduate School of Engineering, Tohoku University
6-3, Aoba, Aoba-ku, Sendai, Miyagi 980-8578, Japan
** 東北大学サイバーサイエンスセンター
〒980-8578　宮城県仙台市青葉区荒巻字青葉6-3
Cyberscience Center, Tohoku University
6-3, Aoba, Aoba-ku, Sendai, Miyagi 980-8578, Japan
*** 東北大学大学院医工学研究科
〒980-8578　宮城県仙台市青葉区荒巻字青葉6-3
Graduate School of Biomedical Engineering, Tohoku University
6-3, Aoba, Aoba-ku, Sendai, Miyagi 980-8578, Japan
**** オリンパス (株)
〒192-8512　東京都八王子市久保山町2-3
Olympus Corporation
2-3, Kuboyama-cho, Hachioji, Tokyo 192-8512, Japan
*5 国立循環器病研究センター研究所
〒565-8565　大阪府吹田市藤白台5–7–1
National Cerebral and Cardiovascular Center Research Institute
5-7-1, Fujishirodai, Suita, Osaka 565-8565, Japan
*6 九州大学大学院医学研究院
〒812-8582　福岡県福岡市東区馬出3-1-1
Graduate School of Medicine, Kyushu University
3-1-1, Maidashi, Higashi-ku, Fukuoka, Fukuoka 812-8582, Japan

占める[2][3]。これらの致死性不整脈は，心疾患を抱えている患者のみならず，健康な子どもや成人のスポーツ選手であっても突如として発症することがある。そこで，近年では，自動体外式除細動器 (AED: Automated External Defibrillator) が学校や公共施設に設置され，その普及によって発症後の救命率が上がっている。一方，このような致死性不整脈は再発率が高いと言われており，致死性不整脈発作を起こした患者の再発後の早期治療システムが必要である。そこで，1960 年代に Mirowski らにより植込み型除細動器 (ICD: Implantable Cardioverter Defibrillator) と呼ばれる装置が提唱され，実用化に至っている[4]。

現在は，洞性頻拍および上室性不整脈 (SVT: supraventricular tachyarrhythmia) などの致死性でない不整脈に対する誤作動を防ぐため，心房内電位もモニタすることで致死性不整脈の鑑別をより確実に行う第 5 世代 ICD が臨床使用されている[5]。しかし，既存の ICD における不整脈検出アルゴリズムでは，主として心電図 (ECG: electrocardiogram) の時間間隔情報に基づいて VF や VT の発生検出を行っているものがほとんどであるため，VF と VT を確実に区別することが困難である。また，一方で ICD が致死的ではない不整脈を誤認して不適切な治療が行われることがあり[6]~[8]，致死性不整脈を的確に検出する ICD の開発が急務とされている。

従来の方法に対し，われわれの研究グループでは，複数の心内心電図信号 (IECG: Intracardiac electrocardiogram) から複数の指標を求め，それらを説明変数とし，不整脈の種類を目的変数とする重回帰モデルを用いる方法を提案し，高精度かつ早期の不整脈検出が可能であることを示してきた[9][10]。この提案方法によって，R-R 間隔以外の情報も用いることで，不整脈をより柔軟に特徴づけることが可能となっている。しかし，それらの研究では，モデルへの入力として用いたデータに含まれる不整脈（SVT, VT, VF）の割合が，正常洞調律 (SR: sinus rhythm) の割合に比べてかなり少なく，このことが誤検出の原因となっていた。そのため，VF の不検出率を 0 に近づけることが難しく，臨床応用上問題となる可能性があった。

そこで，本研究では，不整脈の割合が SR に比べて小さいデータ群において，誤検出の少ない重回帰モデルの作成方法を提案する。さらに，先行研究[10]の方法をさらに発展させることで，VF の不検出率を 0 に近づけるとともに，ICD の誤作動の原因となる誤検出をできるだけ減らすことを目的とする。

2. 方　法

〈2·1〉 実験データとその処理　本研究では，先行研究[9][10]と同様に，5 頭の成犬を対象とした急性実験のデータを用いた。データは，左心室内（$IECG_{LV}$），右心室内（$IECG_{RV}$），および右心房内（$IECG_{RA}$）において取得した心内心電図であり，250 Hz にて再サンプリングを行ったものを用いた。なお，不整脈の自然発生を計測するのは困難であるため，電気刺激によって Fig.1 のように SVT, VT および VF を模擬した。なお，データには 1 度だけ自然発生した VF も含まれている。

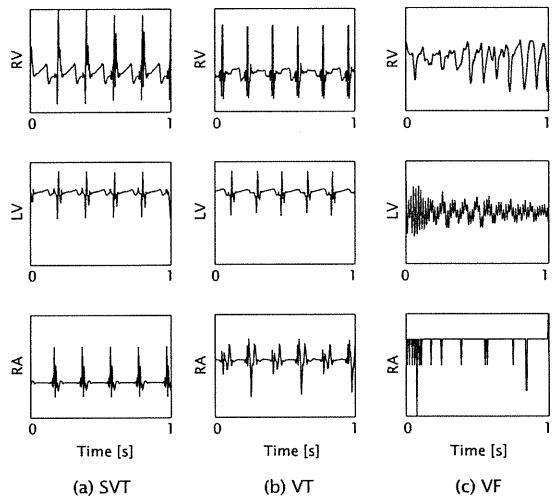

Fig. 1. Examples of IECG signals of (a) SVT, (b) VT, and (c) VF

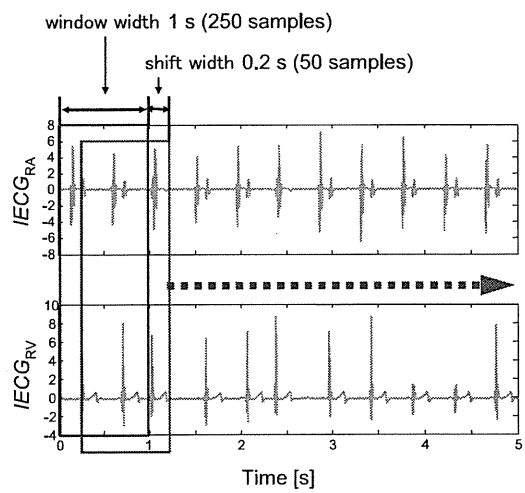

Fig. 2. Data acquisition using a 1 s long window shifting every 0.2 s

最初に，取得した心内心電図データに対して，0.8 Hz~40 Hz の帯域通過型フィルタを用いてノイズ成分を除去した。フィルタ処理後，Fig.2 に示すように，1 s の長さの窓を用いて 0.2 s ずつシフトさせながらデータを抽出した。本研究では，窓ごとに心内心電図の特徴量に基づく指標を算出した。ここで，それぞれの心調律における窓の個数を Table 1 に示す。Table 1 からわかるように，SR が約 67% を占め，その他の心調律の割合が低い。それゆえ，重回帰モデルの推定方法を工夫しないと SR の検出に特化したモデルとなってしまう可能性がある。

(倫理面への配慮)

実験に用いた成犬は，国立循環器病研究センター研究所の倫理委員会の規定に従って適切に管理され，実験は苦痛を与えない麻酔下で行われた。